

Enhanced CeO₂ oxygen defects decorated with AgInS₂ quantum dots form an S-scheme heterojunction for efficient photocatalytic selective oxidation of xylose

Aohua Li ^a, Jiliang Ma ^{a,*}, Min Hong ^b, Runcang Sun ^{a,*}

^a Liaoning Key Lab of Lignocellulose Chemistry and BioMaterials, Liaoning Collaborative Innovation Center for Lignocellulosic Biorefinery, College of Light Industry and Chemical Engineering, Dalian Polytechnic University, Dalian 116034, China

^b Centre for Future Materials, University of Southern Queensland, Springfield Central Queensland, 4300, Australia



ARTICLE INFO

Keywords:
 S-scheme heterojunction
 Oxygen vacancies
 Xylic acid
 CO
 Photocatalytic biorefinery

ABSTRACT

S-scheme heterojunctions have become an emerging type of effective photocatalysts to convert biomass. However, there are few reports on the synergistic S-type heterojunction and oxygen vacancy enhanced photocatalytic biomass conversion. Here, an AgInS₂@CeO_{2-x} S-scheme heterojunction photocatalyst with abundant oxygen vacancies was developed through a simple thermal and mild annealing process, allowing for the simultaneous production of xylic acid and CO. Under visible light, the xylic acid yield and CO evolution rate reached 60.0% and 3689.9 $\mu\text{mol g}^{-1} \text{h}^{-1}$, respectively, through the decomposition of xylose. It was found that the S-scheme staggered band structure could improve sunlight utilization, increase the reduction power of photo-generated electrons, and enhance the separation and transfer of photogenerated charge carriers. Furthermore, oxygen vacancies on the surface of CeO₂ for AgInS₂@CeO_{2-x} heterojunction can suppress the recombination of generated electrons and holes. This study offers a promising approach for designing artificial photosynthetic systems to promote photocatalytic biomass conversion.

1. Introduction

As the only renewable carbon source in nature, biomass stores solar energy and carbon through photosynthesis [1,2]. The abundance of chemicals and fuels are converted from biomass. Photocatalysis is a promising strategy to produce value-added chemicals, which has attracted increasing attention [3,4]. Various photocatalytic processes and photocatalysts have been developed for biomass conversion to produce hydrogen, liquid fuels, and other chemicals [5–7]. Xylic acid, which is a biomass-derived acid, was listed by the US Department of Energy as one of the thirty most potential compounds [8]. Meanwhile, photocatalytic biorefinery is an important pathway to produce xylic acid [9].

Compared with traditional high-temperature chemical and biological methods, photocatalytic technology has diversified advantages, such as mild reaction conditions, high efficiency, and low energy consumption [10]. For example, Liu et al. employed carbon aerogel material (α -TiO₂@MC) by anchoring chitosan and sodium carboxymethylcellulose. The xylic acid yield reached its maximum (52.26%) from xylose

under visible light irradiation [11]. Nevertheless, the above research only focuses on the liquid products in the reaction without gas products. In previous reports, Wang et al. dispersed Cu on titanium oxide nanorods for the selective conversion of biomass-derived sugars into CO [5]. Zhang et al. reported 1213.88 $\mu\text{mol g}^{-1} \text{h}^{-1}$ CO evolution during the photocatalytic process of producing xylic acid from xylose using CIS/GO@3D-OMA photocatalyst [12]. These reported research findings suggest that the co-production of xylic acid and CO in the photocatalytic biorefinery process is a feasible process, which improves atomic utilization. To achieve this, it is essential to design a photocatalyst with high selectivity and activity.

In the past decades, rare earth metal oxide materials have shown tremendous capabilities in efficient and cost-effective photocatalysis for various reactions due to their unique physical and chemical properties [13]. Cerium oxide (CeO₂) is regarded as one of the most promising photocatalysts, due to high structural stability, low cost, and excellent redox ability [14,15]. The rich surface chemical features of CeO₂ including Lewis acidic site, Lewis basic site, Bronsted acidic site, and oxygen vacancy provide an ideal platform to understand the influence of

* Corresponding authors.

E-mail addresses: jlma@dlpu.edu.cn (J. Ma), rcsun3@dlpu.edu.cn (R. Sun).

adsorption behavior on the catalytic performance of CeO_2 -based heterogeneous catalysts. Oxygen vacancies and Ce^{3+} ions in ceria can improve oxygen gas adsorption and activation as well as oxygen self-diffusion in the lattice of nonstoichiometric ceria, benefiting the redox process and catalytic reaction [16]. Serving as electron donors, oxygen vacancies improve electron migration in the photocatalytic process [17,18]. The formation of oxygen vacancies can be controlled by rationally tuning thermal-treatment temperature and oxygen partial pressure, doping elements and content, synthesis methods, surface stress, and electrical field [16]. Nevertheless, the wide bandgap and low visible light utilization hinder CeO_2 as efficient photocatalysts [19,20]. Additionally, a single photocatalyst cannot reserve both the strong oxidation ability of holes and the strong reduction ability of electrons due to band structure limitations [21].

It is challenging to develop an efficient photocatalytic system that simultaneously exhibits visible light responses, effective charge separation and strong redox capabilities. In this regard, constructing an S-scheme heterojunction composed of reduction photocatalysts (RP) and oxidation photocatalysts (OP) is a promising strategy for improving photocatalytic efficiency. S-scheme heterojunction has proven to be a superior junction system with a strong built-in electric field, which facilitates the separation of electron-hole pairs and maintains their high redox ability [22]. When RP and OP come into contact without light irradiation, band bending and an internal electric field appear at the interface of the two semiconductor contacts. Upon light irradiation, electrons are excited to form electron-rich and hole-rich regions in RP and OP, respectively. Driven by an internal electric field, the photo-generated electrons on the conduction band (CB) of OP consume holes on the valence band (VB) of RP. Simultaneously, photo-generated electrons and holes with strong redox abilities are increasingly retained on the CB of RP and the VB of OP, ensuring the high redox ability of S-scheme heterojunctions [23,24].

One typical example to demonstrate the highly efficient photocatalyst of S-scheme heterojunctions is Ni@6MOF/BiVO_4 , prepared using an H-bonding-induced assembly process [25]. The CO_2 photo-conversion of Ni@6MOF/BiVO_4 was reported to be 66 times higher than that of BiVO_4 nanoparticles in pure water, because of the favorable charge separation under the positive influence of S-scheme heterojunctions. Moreover, You et al. developed a hollow structured S-scheme heterojunction named h-ZnSe/Pt@TiO_2 to produce H_2 and formic acid in pure water. The productivities of H_2 and formic acid reached 1858 and 372 $\mu\text{mol g}^{-1} \text{h}^{-1}$, respectively, for over 300 h [26].

AgInS_2 quantum dots (QDs), typical reduction photocatalysts (RP), have garnered increasing interest in the field of photocatalytic degradation, originating from AgInS_2 featured by high chemical stability, tunable band structure and excellent visible light response [27,28]. Furthermore, QDs exhibit better electron-hole pairs separation compared with bulk materials due to the short electron-hole diffusion distance [29,30]. Previous studies have demonstrated that constructing heterojunctions via incorporating pure AgInS_2 with additional compatible photocatalysts can effectively improve the photocatalytic activity [31].

In this study, we have devised a 0D/3D S-scheme heterojunction involving CeO_2 adorned with AgInS_2 QDs to improve the photocatalytic efficiency using straightforward two-step hydrothermal and mild annealing processes. Electron paramagnetic resonance (EPR) analysis has confirmed the increased oxygen vacancies in the successfully constructed S-scheme heterojunction, which serve as electron donors to favor the photocatalytic performance. Moreover, staggered band structures with distinct Fermi levels between AgInS_2 QDs and CeO_2 effectively enhances charge separation. Accordingly, our S-scheme heterojunction yields superior photocatalytic performance, resulting in the highly efficient production of xylonic acid (60.0%) and CO (3689.9 $\mu\text{mol g}^{-1} \text{h}^{-1}$). The underlying charge transfer mechanism in S-scheme is elucidated through *in-situ* X-ray photoelectron spectroscopy (*in-situ* XPS) and Kelvin probe force microscopy (KPFM) spectra. This study offers a

promising approach for developing defect-rich S-scheme photocatalysts for the production of biomass-derived chemicals and fuels via photocatalytic biomass refining.

2. Experimental section

2.1. Preparation of CeO_2

First, 4 mL of *N*-butyl silicate, 60 mL of ethanol, and 9 mL of ammonia solution were mixed with 100 mL of deionized water, followed stirring for 1 h. The mixed solution was centrifuged at 5000 rpm for 10 min to obtain SiO_2 . The collected powder was dried at 60 °C for 8 h to obtain SiO_2 . Afterward, 0.15 g of SiO_2 were added to 30 mL of ethanol and sonicated for 30 min to obtain a homogeneous suspension, referred to as suspension A. Next, 2.6 g of $\text{Ce}(\text{NO}_3)_3 \cdot 6 \text{ H}_2\text{O}$ and 0.8 g of urea were dissolved in 50 mL of deionized water to create solution B. Suspension A and solution B were thoroughly mixed in a stainless-steel autoclave and treated at 160 °C for 8 h in an Ar atmosphere. At the end of the reaction, the white powder of $\text{SiO}_2@\text{CeO}_2$ was obtained after centrifugation and drying. Finally, 2 g of $\text{SiO}_2@\text{CeO}_2$ was added to 80 mL of 2 M KOH and treated in a beaker using a water bath at 80 °C for 2 h. These steps should be repeated six times. After drying at 60 °C for 4 h, the powder was annealed at 600 °C for 2 h in an air atmosphere to obtain the yellow powder of CeO_2 .

2.2. Preparation of AgInS_2 QDs

1.1678 g of indium acetate, 12.2928 g of glutathione, 0.6748 g of silver nitrate, and 10 mL of an 8 mM Na_2S solution were added into 250 mL of deionized water. The pH of resulting mixture was adjusted to 8.0 using a concentrated NaOH solution. Subsequently, the solution was treated in a round-bottom flask in an oil-bath at 100 °C for 3.5 h. After chilling to the room temperature, an excess of ethanol was added to the solution to precipitate AgInS_2 QDs. Next, the mixture was centrifuged at 8000 rpm for 10 min to obtain a black precipitate. The black precipitate was then washed several times with deionized water and ethanol. Finally, the black powder AgInS_2 QDs were obtained through the process of drying.

2.3. Preparation of $\text{AgInS}_2@\text{CeO}_2-x$ photocatalysts

0.5 g of CeO_2 and a specific amount of AgInS_2 QDs were added into 10 mL of deionized water. The mixture was evaporated to dryness at 90 °C to give a dry powder. Subsequently, the blend of CeO_2 and AgInS_2 QDs was annealed at 200 °C for 20 min in an Ar atmosphere to produce the $\text{AgInS}_2@\text{CeO}_2-x$ heterostructure. The mass ratios of AgInS_2 QDs to CeO_2 were 5%, 10%, 20%, and 30%, respectively. Correspondingly, the resulting materials were labeled as $\text{AgInS}_2@\text{CeO}_2-5$, $\text{AgInS}_2@\text{CeO}_2-10$, $\text{AgInS}_2@\text{CeO}_2-20$, and $\text{AgInS}_2@\text{CeO}_2-30$, respectively.

2.4. Photocatalytic co-production of xylonic acid and CO from xylose

Typically, 10 mg of $\text{AgInS}_2@\text{CeO}_2-x$ and 200 mg of xylose were added into 20 mL of a KOH aqueous solution. The photocatalytic co-production of CO and xylonic acid was carried out under visible light irradiation using the Perfectlight PCX 50 C multi-channel photocatalytic reaction system, with varying reaction temperatures, irradiation times, and alkali concentrations. Finally, the resulting liquid product and the generated CO were analyzed using high-performance liquid chromatography (HPLC) and gas chromatography (GC), respectively.

2.5. Poisoning experiments

Typically, 10 mg of $\text{AgInS}_2@\text{CeO}_2-20$, 200 mg of xylose and 20 mmol of sacrificial agents (tryptophan (Trp), *p*-phthalic acid (PTA), *p*-benzoquinone (BQ), and ethylenediaminetetraacetic acid (EDTA)) were added

into 20 mL of a 0.1 M KOH solution. The reaction was conducted under visible light irradiation at approximately 60 °C for 1 h. Finally, the resulting liquid product and the generated CO were analyzed using the methods mentioned above.

2.6. Recycling experiments

The methods of recycling experiments were the same as described above. In each cycle, 10 mg of AgInS₂@CeO₂-20 and 200 mg of xylose was added into 20 mL of a 0.1 M KOH solution. The reaction was irradiated by visible light at ~ 60 °C for 1 h. The obtained liquid product and the generated CO were analyzed using the methods mentioned previously. At the end of each cycle, the system was centrifuged at 5000 rpm for 10 min to recover AgInS₂@CeO₂-20. Meanwhile, HPLC and GC were used to analyze the produced liquid product and CO for each cycle.

3. Results and discussion

3.1. Catalyst preparation and characterizations

Fig. 1 illustrates the two-step hydrothermal and mild annealing processes for preparing AgInS₂@CeO₂-x, involving the loading of AgInS₂ QDs to form a tightly bonded heterojunction. Photocatalysts with varying mass ratios of AgInS₂ QDs and CeO₂ were prepared and named AgInS₂, CeO₂-x, AgInS₂@CeO₂-5, AgInS₂@CeO₂-10, AgInS₂@CeO₂-20, and AgInS₂@CeO₂-30, respectively. The microscopic morphologies of the prepared samples were investigated using scanning electron microscopy (SEM) and transmission electron microscopy (TEM). Figs. 2A, 2B and S1A depict that the AgInS₂@CeO₂-20 shows a hexahedral block structure formed by arrangement of nanospheres. CeO₂ exhibits a layered block like structure with nanospheres arrangement (Fig. S1B and S1C). Fig. S2 displayed the N₂ sorption isotherms of CeO₂, and SiO₂@CeO₂. All of them exhibited type IV isotherm patterns, suggesting the existence of numerous mesopores in these samples. Compared to the SiO₂@CeO₂ (15.7 m²/g), the specific surface area (28.9 m²/g) of CeO₂ was greatly enhanced after the removal of SiO₂, which created more mesopores. The enhanced specific surface area could facilitate the diffusion of xylose into photocatalysts. As shown in Fig. S3, the presence of Ag, In, and S elements was detected in the AgInS₂@CeO₂-20, confirming the successful introduction of AgInS₂ QDs.

TEM image and high-resolution TEM (HRTEM) images of AgInS₂ QDs (Figs. 2C and 2D), its size ranges from 3 to 5 nm [32], while its lattice fringes with *d*-spacing of 0.173 nm correspond to the (322) crystal plane of AgInS₂ QDs. Furthermore, HRTEM image (Fig. 2E) of

AgInS₂@CeO₂-20 confirm the formation of heterogeneous structures, identifying the crystalline phases of AgInS₂ QDs and CeO₂, respectively. The *d*-spacing value of 0.173 nm in AgInS₂ QDs corresponds to the (322) crystal plane, while the 0.312 nm *d*-spacing in CeO₂ corresponds to the (111) crystal plane [33] (Fig. 2F). To further investigate the loading of AgInS₂ QDs, energy-dispersive X-ray spectroscopy (EDX) analysis was performed, confirming the successful introduction of all elements (Ag, In, and S) from the AgInS₂ QDs (Fig. 2J-L). Fig. 2N presents X-ray diffraction (XRD) patterns for CeO₂, AgInS₂ QDs, AgInS₂@CeO₂-5, AgInS₂@CeO₂-10, AgInS₂@CeO₂-20, and AgInS₂@CeO₂-30. Pristine CeO₂ exhibits four typical diffraction peaks at 28.4°, 33.0°, 47.4°, and 56.4°, attributed to the (111), (200), (220), and (311) crystal planes of CeO₂ (JCPDS No.34-0394), respectively [33]. The diffraction peaks of AgInS₂ QDs match those of standard orthorhombic AgInS₂ crystals (JCPDS No.25-1328) [34]. Notably, no diffraction peaks of AgInS₂ are observed in the XRD pattern of AgInS₂@CeO₂-x due to the low crystallinity of AgInS₂ QDs [35].

X-ray photoelectron spectroscopy (XPS) was conducted to further investigate chemical composition and state of elements in the prepared photocatalysts. The XPS survey spectrum of AgInS₂@CeO₂-20 confirmed the presence of Ce, O, Ag, In, and S (Fig. S4). As shown in Fig. 3A, several peaks in CeO₂, located at 916.5 eV, 907.4 eV, 900.7 eV, 898.1 eV, 888.8 eV, and 882.3 eV, were attributed to Ce (IV) species, while the peaks at 902.4 eV and 884.9 eV in CeO₂ were associated with Ce (III) species [36]. Notably, after the heterojunction was formed between AgInS₂ QDs and CeO₂, the binding energy of Ce (III) species in the AgInS₂@CeO₂-20 complex decreased as compared with CeO₂. This suggests that in the absence of illumination, the CeO₂ acts as an e⁻ acceptor in AgInS₂@CeO₂-20 complex. Interestingly, the peak area ratios of Ce (III) to Ce (IV) in CeO₂ and AgInS₂@CeO₂-20 were calculated to be 5.28% and 36.84%, respectively. A high ratio of Ce (III) to Ce (IV) is advantageous for creating abundant oxygen vacancies, thereby enhancing photocatalytic activity [37]. Oxygen vacancies can function as e⁻ or h⁺ capture sites, improving charge separation by restraining the recombination of h⁺-e⁻ pairs [38]. The O 1 s spectrum of CeO₂ can be fitted with two peaks at 532.0 eV and 529.3 eV, attributing to surface oxygen vacancies (O_v) and lattice oxygen (O_{lat}), respectively (Fig. 3B) [39,40]. Evidently, the peak area of O_v species in AgInS₂@CeO₂-20 (69.6%) is higher than that in CeO₂ (46.19%), primarily due to the higher concentration of Ce (III) species on the AgInS₂@CeO₂-20 leading to the formation of oxygen vacancies. To further confirm the existence of O_v, electron paramagnetic resonance (EPR) technology was employed (Fig. 3C). Both the CeO₂ and AgInS₂@CeO₂-20 sample exhibited EPR signals centered at g = 2.003, indicative of e⁻ trapped at O_v. The noticeable increase in the signal peak intensity of AgInS₂@CeO₂-20

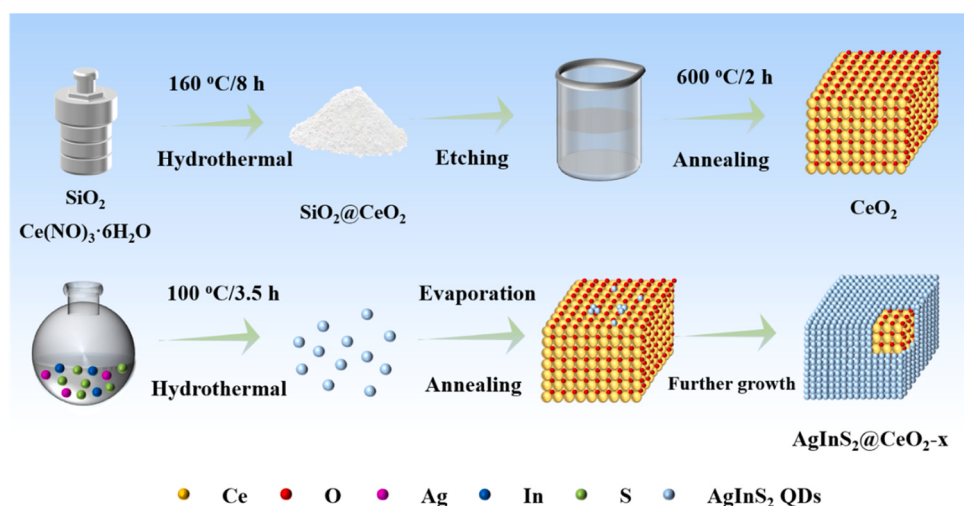


Fig. 1. The schematic illustration of fabricating AgInS₂@CeO₂-x.

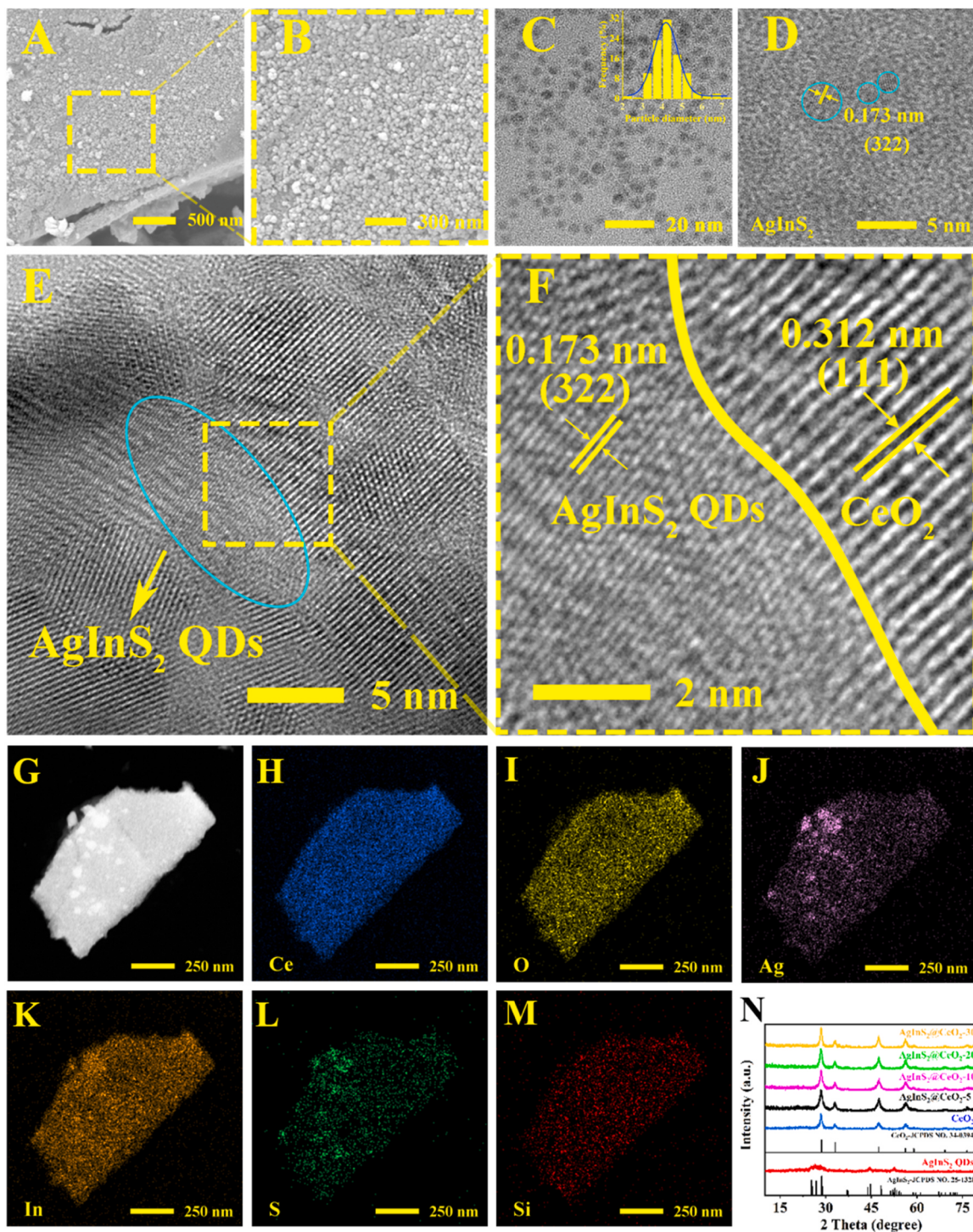


Fig. 2. SEM images of AgInS₂@CeO₂-20 (A and B). TEM image (C) and HRTEM image (D) of AgInS₂ QDs. HRTEM images of AgInS₂@CeO₂-20 (E and F). The HADDF-STEM image (G) and the EDX mapping images (H-M) of AgInS₂@CeO₂-20. The XRD patterns of CeO₂, AgInS₂ QDs, and AgInS₂@CeO₂-x (N).

suggests an increase in O_v, implying the role of mild annealing [41]. The Ag 3d spectrum in AgInS₂ QDs reveals two peaks at 373.7 eV and 367.7 eV, attributed to Ag 3d_{3/2} and Ag 3d_{5/2}, respectively (Fig. 3D). As displayed in Fig. 3E, the peaks at 452.2 eV and 444.6 eV in the In 3d spectrum of AgInS₂ QDs correspond to In 3d_{3/2} and In 3d_{5/2} for In³⁺, respectively [42]. The S 2p spectrum of AgInS₂ QDs can be deconvoluted into two characteristic peaks at 162.5 eV and 160.9 eV (Fig. 2F), assigning to S 2p_{1/2} and S 2p_{3/2} for S²⁻, respectively [43]. Remarkably, in comparison to AgInS₂, the binding energies of Ag 3d, In 3d and S 2p in AgInS₂@CeO₂-20 increased, which may be attributed to the interfacial

interactions between AgInS₂ QDs and CeO₂ [44]. These results further confirm the successful preparation of AgInS₂@CeO₂-20.

3.2. Optical and electrical properties

To evaluate the light absorption characteristics of the prepared samples, ultraviolet-visible diffuse reflectance absorption spectra (UV-vis DRS) were employed. As exhibited in Fig. 4A, the absorption edge of CeO₂ is observed at approximately 560 nm. After introducing AgInS₂ QDs, an evident redshift of the absorption edge is observed in

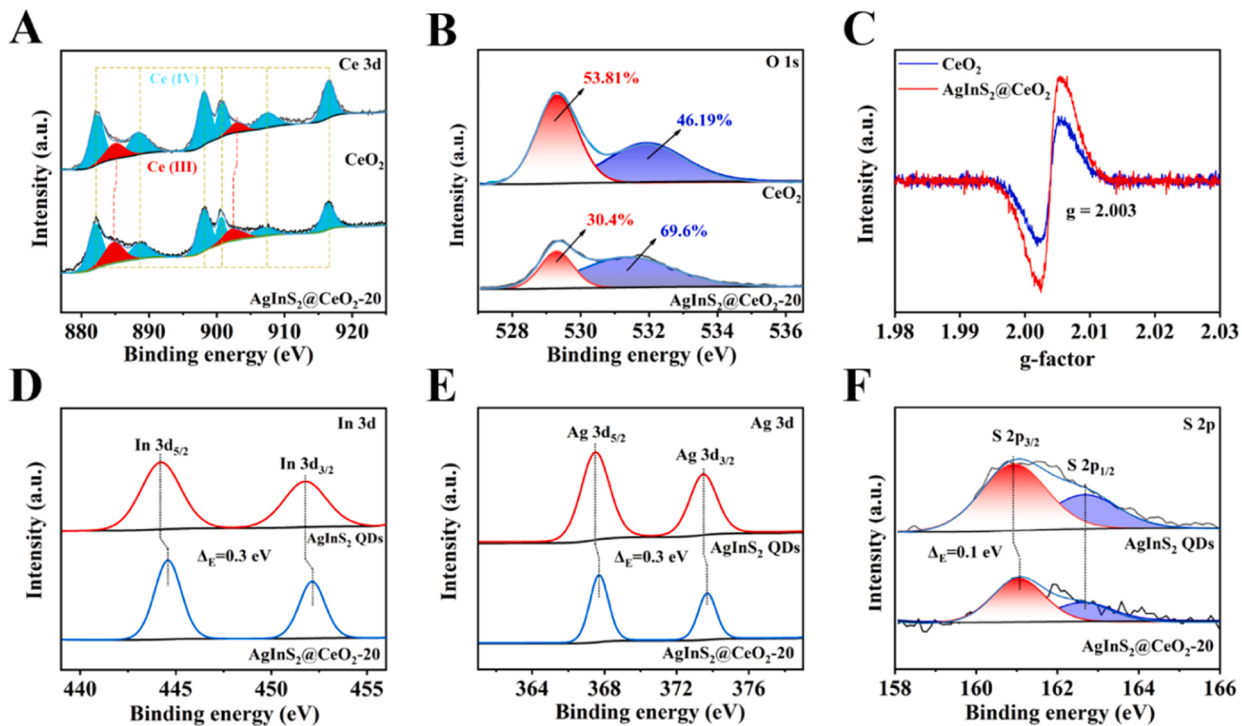


Fig. 3. High-resolution ex-situ XPS spectra of Ce 3d (A) and O 1 s (B) for CeO₂ and AgInS₂@CeO₂-20, along with Ag 3d (D). EPR spectra of CeO₂ and AgInS₂@CeO₂-20 (C). High-resolution XPS spectra of In 3d (E) and S 2p (F) for AgInS₂ QDs and AgInS₂@CeO₂-20.

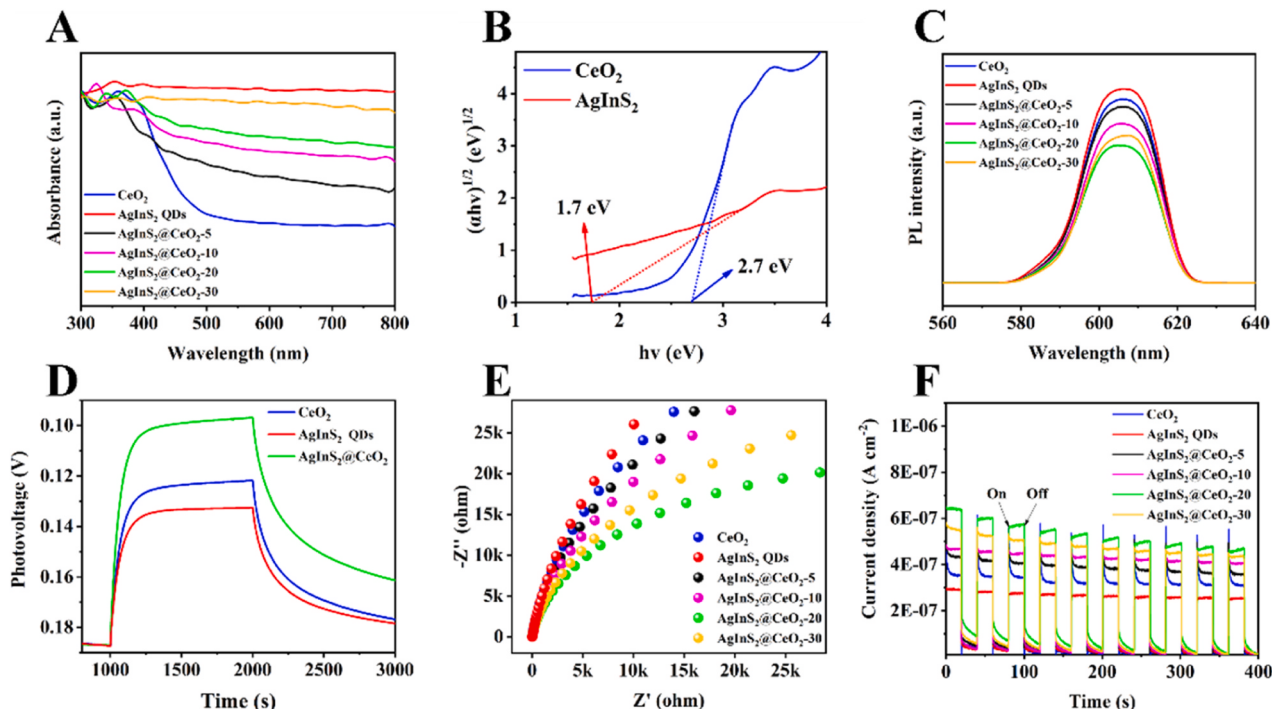


Fig. 4. The UV-vis DRS of CeO₂, AgInS₂ QDs, and AgInS₂@CeO₂-x (A). The plots of the transformed Kubelka-Munk function versus photo energy for CeO₂ and AgInS₂ QDs (B). The PL spectra of CeO₂, AgInS₂ QDs, and AgInS₂@CeO₂-x (C). The OCVD of CeO₂, AgInS₂ QDs, and AgInS₂@CeO₂-20. The EIS curves (E) and photocurrent response plots (F) of CeO₂, AgInS₂ QDs, and AgInS₂@CeO₂-x.

AgInS₂@CeO₂-x, indicating that the introduction of AgInS₂ QDs improves the absorption of photocatalysts in the visible light and near-infrared region. Notably, AgInS₂@CeO₂-20 can capture light at all wavelengths. The bandgaps of CeO₂ and AgInS₂ QDs are calculated as 2.7 eV and 1.7 eV from plots of the transformed Kubelka-Munk function

versus photo energy (Fig. 4B). As we known, charge recombination hinders photo-generated h⁺-e⁻ pairs from effectively participating in the redox reaction, significantly impeding photocatalytic processes. Steady-state photoluminescence (PL) spectroscopy was carried out to investigate charge recombination. As depicted in Fig. 4C, the PL intensity of

$\text{AgInS}_2@\text{CeO}_2$ -20 is the lowest among all sample, indicating the weakest charge recombination [45]. As shown in Fig. S5, the oxygen vacancies of CeO_2 generate electron trapping states during the photocatalytic process [46]. The trap states can form more easily due to the presence of oxygen vacancies, which can trap a portion of excited electrons to partially inhibit direct recombination of the photogenerated carriers. As shown in the open-circuit voltage decay (OCVD) in Fig. 4D, $\text{AgInS}_2@\text{CeO}_2$ -20 exhibits the strongest photo-voltage and slowest photovoltage decay, indicating the highest carrier concentration and longest carrier lifetime. In the photocatalytic process, a long carrier lifetime enables photo-generated $\text{h}^+ \text{e}^-$ pairs to come into more extensive contact with the reactants. To investigate the charge transfer in each photocatalyst, electrochemical impedance spectroscopy (EIS) was carried out. As displayed in Fig. 4E, the impedance of all $\text{AgInS}_2@\text{CeO}_2$ -x samples is lower than that of CeO_2 and AgInS_2 QDs after combing AgInS_2 QDs. Moreover, $\text{AgInS}_2@\text{CeO}_2$ -20 shows the lowest impedance, indicating that an S-scheme heterojunction is beneficial for carrier transfer. As shown in the transient photocurrent response plot (Fig. 4F), a similar result with the EIS can be observed. The photocurrent intensity of $\text{AgInS}_2@\text{CeO}_2$ -20 is 1.8 and 2.2 times higher than that of CeO_2 and AgInS_2 QDs, respectively, confirming rapid carrier separation under the positive influence of S-scheme heterojunctions.

3.3. Photocatalytic activity of $\text{AgInS}_2@\text{CeO}_2$ -x

The photocatalytic performance of CeO_2 , AgInS_2 QDs, and $\text{AgInS}_2@\text{CeO}_2$ -x was assessed under visible light irradiation. Initially, the photocatalytic performances of various photocatalysts were compared in a 0.3 M KOH solution at 50 °C for 3 h. Fig. 5 A shows that the xylonic acid yield and CO evolution rate tends to increase with the addition of different photocatalyst. To determine the optimal reaction parameters, the effects of reaction temperature, reaction time, and alkali concentration were investigated. Fig. 5B displays the impact of reaction temperature, with the highest yield (45.1%) of xylonic acid obtained at

60 °C. The CO evolution rate displayed a volcano-like trend, reaching the highest value of 3199.4 $\mu\text{mol g}^{-1} \text{h}^{-1}$ at 50 °C. However, at high temperature, lactic acid and other by-productions were released in significant quantities due to the overoxidation of xylonic acid (Fig. S6B). In addition, the reaction under dark conditions was performed (Fig. S7). The yield of xylonic acid was only 32.9% and CO production of only 1625.26 $\mu\text{mol g}^{-1} \text{h}^{-1}$ at 60 °C in the dark, indicating a possible minor photothermal process [47]. Noteworthy, photocatalysis is the dominating process to ensure highly efficient productions of xylonic acid and CO, proving the superior photocatalytic performance of the as-developed S-scheme heterojunction. The yield of xylonic acid and CO evolution rate exhibited similar trends (Fig. 5 C). The maximum values for the xylonic acid yield and CO evolution rate were 49.7% and 3601.8 $\mu\text{mol g}^{-1} \text{h}^{-1}$ at 60 min, respectively, before gradually decreasing. With increasing reaction time, the production of by-products increased, like because xylonic acid was degraded into small molecular products (Fig. S6C). Finally, the influences of alkali concentration in the reaction system were investigated. The xylonic acid yield reached its peak at 60.0% in 0.1 M KOH (Fig. 5D). In system with high alkali concentration, an excess of $\cdot\text{OH}$ radicals may oxidize xylonic acid into other organic acid, leading to a reduction in yield (Fig. S6D). Similarly, CO showed the highest evolution rate (3689.9 $\mu\text{mol g}^{-1} \text{h}^{-1}$) in 0.1 M KOH solution. Notably, the yield of xylonic acid (60.0%) using $\text{AgInS}_2@\text{CeO}_2$ -20 was 3.2 times higher than that in a photocatalyst-free system (18.9%), implying the indispensable role of the $\text{AgInS}_2@\text{CeO}_2$ -20 photocatalyst (Fig. S7). Moreover, the $\text{AgInS}_2@\text{CeO}_2$ -20 photocatalyst exhibited good cycling stability over five consecutive photocatalytic cycles and no significant change in chemical composition (Figs. 5E and 5 F). As shown in Fig. S8, electron paramagnetic resonance (EPR) technology was employed. Both the fresh and recycled $\text{AgInS}_2@\text{CeO}_2$ -20 sample exhibited EPR signals centered at $g = 2.003$, despite the slightly decreased peak intensity upon recycling. This result suggests excellent stability of $\text{AgInS}_2@\text{CeO}_2$ -20.

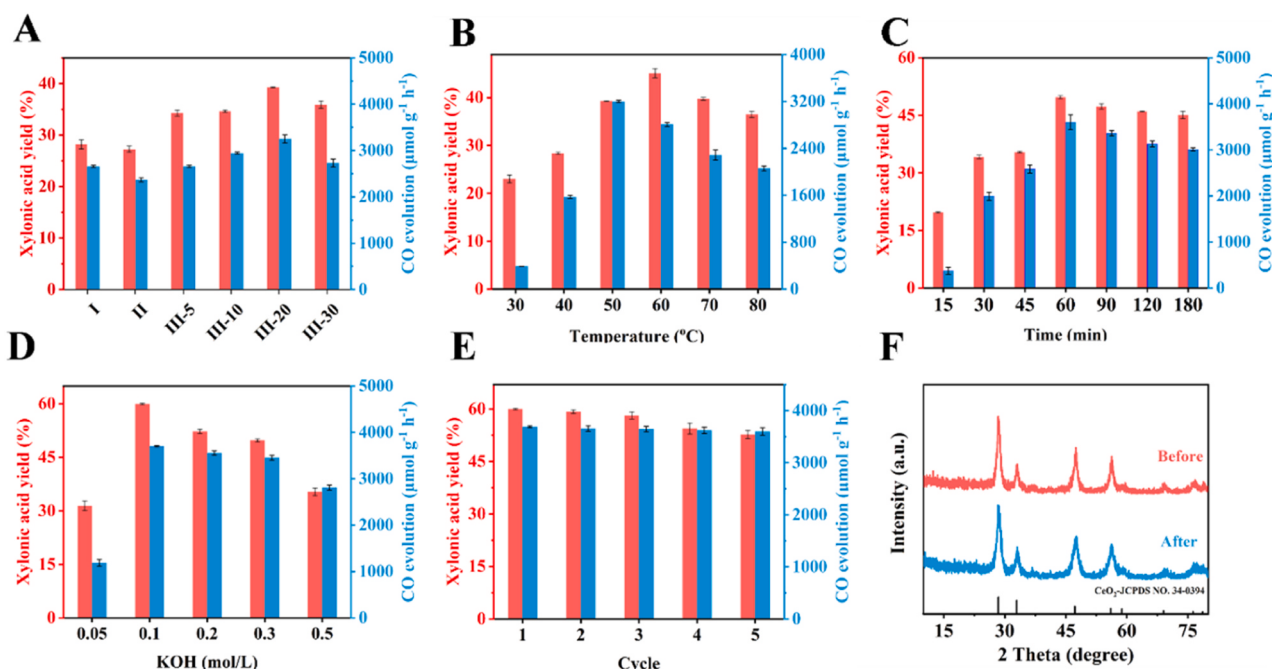


Fig. 5. (A) The photocatalytic conversion of xylose using different samples under visible light irradiation (xylose: 200 mg, samples: 10 mg, KOH solution: 0.30 M, 20 mL, irradiation time: 3 h, reaction temperature: 50 °C). Notes: I: CeO_2 ; II: AgInS_2 QDs; III: $\text{AgInS}_2@\text{CeO}_2$ -5, 10, 20, and 30. The effects of reaction temperatures (B) (xylose: 200 mg, $\text{AgInS}_2@\text{CeO}_2$ -20: 10 mg, KOH solution: 0.3 M, 20 mL, irradiation time: 3 h), irradiation time (C) (xylose: 200 mg, $\text{AgInS}_2@\text{CeO}_2$ -20: 10 mg, KOH solution: 0.30 M, 20 mL, reaction temperature: 60 °C) and KOH concentrations (D) (xylose: 200 mg, $\text{AgInS}_2@\text{CeO}_2$ -20: 10 mg, irradiation time: 1 h, reaction temperature: 60 °C, KOH solution: 0.1 mol/L). (E) The recycling test (xylose: 200 mg, $\text{AgInS}_2@\text{CeO}_2$ -20: 10 mg, irradiation time: 1 h, reaction temperature: 60 °C, KOH solution: 0.1 mol/L). (F) The XRD patterns of fresh and recycled $\text{AgInS}_2@\text{CeO}_2$ -20.

3.4. Catalytic mechanism of $\text{AgInS}_2@\text{CeO}_2\text{-}x$

To detect the radicals generated during the reaction and assess the redox capabilities of $\text{AgInS}_2@\text{CeO}_2\text{-}20$, ESR characterizations were performed. Three capture agents were used to prove the existence of photo-generated e^- , h^+ , $\cdot\text{O}_2$, $\cdot\text{OH}$, and $^1\text{O}_2$ in the ESR spectrum of $\text{AgInS}_2@\text{CeO}_2\text{-}20$. 2,2,6,6-tetramethylpiperidine-*N*-oxyl (TEMPO) was employed to capture e^- and h^+ . As shown in Figs. 6A and 6B, the TEMPO signals weakened with increasing irradiation time, suggesting the presence of e^- and h^+ . Similarly, the capture agents 5,5-dimethyl-1-pyrroline-*N*-oxide (DMPO) were utilized to detect the generation of $\cdot\text{O}_2$ and $\cdot\text{OH}$. Under light and catalyst conditions, the signals of DMPO- $\cdot\text{O}_2$ and DMPO- $\cdot\text{OH}$ adducts appeared and increased. The DMPO- $\cdot\text{O}_2$ signal was observed, and the signal intensity was 1:1:1:1 (Figs. 6C and 6D). Additionally, the signal intensity of DMPO- $\cdot\text{OH}$ was 1:2:2:1. These results suggest that $\cdot\text{O}_2$ and $\cdot\text{OH}$ are produced in the system with $\text{AgInS}_2@\text{CeO}_2\text{-}20$ under light irradiation. Similarly, 2,2,6,6-tetramethyl-4-piperidone-1-oxyl (TEMPONE) was used as a capture agent to detect $^1\text{O}_2$. Triplet peaks with equal intensity appeared under light irradiation, indicating the presence of $^1\text{O}_2$ in the system (Fig. 6E). A poisoning experiment was conducted to assess the impact of active oxidation species. Various sacrificial agents (e.g. Trp, PTA, BQ, EDTA) were employed to remove these species. As shown in Fig. 6F, the introduction of these sacrificial agents resulted in changes in the yield of xylylic acid and CO evolution rate: 45.5%/1696.4 $\mu\text{mol g}^{-1} \text{h}^{-1}$ (Trp), 38.1%/1116.7 $\mu\text{mol g}^{-1} \text{h}^{-1}$ (TPA), 26.2%/614.7 $\mu\text{mol g}^{-1} \text{h}^{-1}$ (BQ), 1.3%/286.1 $\mu\text{mol g}^{-1} \text{h}^{-1}$ (EDTA). These results suggest that the influence of h^+ is greater than those of $^1\text{O}_2$, $\cdot\text{OH}$, and $\cdot\text{O}_2$.

In this study, the Mott-Schottky (M-S) analysis was employed to determine the conduction band (CB) energy level. The flat band potentials of AgInS_2 QDs and CeO_2 were -1.27 and -0.68 V vs. Ag/AgCl , respectively (Fig. 7A). The positive slopes of AgInS_2 QDs and CeO_2 indicated that they were both n-type semiconductors. For n-type semiconductors, the flat band potential was positive 0.2 V as compared with CB. Thus, the CBs of AgInS_2 and CeO_2 were -1.27 V and -0.68 V vs. normal hydrogen electrode (NHE), respectively, using the Nernst

formula ($E_{\text{NHE}} = E_{\text{Ag}/\text{AgCl}} + 0.197$, pH = 7). The valence band (VB) position was determined through VB-XPS analysis. As displayed in Fig. 7B, the VBs of CeO_2 and AgInS_2 QDs were 2.1 V and 0.46 V, respectively. The work function (Φ) of semiconductors was calculated using ultraviolet photoelectron spectroscopy (UPS). Fig. 7C revealed that the Φ of AgInS_2 QDs and CeO_2 were calculated to be 3.59 eV (= 21.20–17.61 eV) and 3.92 eV (= 21.20–17.28 eV), respectively, with 21.20 eV being the energy of UV excitation. Meanwhile, the Fermi level (E_f) can be calculated using the formula: ($E_f = \Phi - 4.44$ eV), where 4.44 eV is the difference between the vacuum level and NHE. Thus, the E_f of AgInS_2 QDs and CeO_2 are calculated to -0.85 V and -0.52 V vs. NHE. Therefore, the staggered band structure of CeO_2 and AgInS_2 QDs is depicted in Fig. 7G (i). As compared with CeO_2 , AgInS_2 QDs have a higher Φ , indicating its stronger ability to bind electrons (e^-). The carrier migration path was investigated via the *ex-situ* and *in-situ* XPS analysis. According to the *ex-situ* XPS results (Fig. 3A and D-F), the binding energies of Ce 3d shifted negatively, while the binding energy of Ag 3d, In 3d, and S 2p shifted positively, suggesting that carriers in AgInS_2 QDs flowed to CeO_2 until E_f is balanced. These results in the positive and negative charge accumulation around the interface of AgInS_2 QDs and CeO_2 , respectively, leading to the presence of an internal electric field. Furthermore, the band edges of AgInS_2 QDs and CeO_2 bend upwards and downwards (Fig. 7G (ii)), respectively. As shown in Fig. 7D-F, under UV lamp irradiation, the binding energies of Ag 3d, In 3d, and Ce 3d shifted negatively and positively, respectively, indicating that carriers migrate from CeO_2 to AgInS_2 QDs. Under light irradiation, the photo-generated e^- in the CB of CeO_2 recombines with the holes in the VB of AgInS_2 QDs. As a result, highly reducing e^- in the CB of AgInS_2 QDs and highly oxidizing h^+ in the VB of CeO_2 are retained, participating in reactions on the surface of the photocatalyst (Fig. 7G (iii)). The Kelvin probe force microscope (KPFM) and atomic force microscope (AFM) were used to further verify the existence of an interfacial electric field and the direction of electron transfer in $\text{AgInS}_2@\text{CeO}_2\text{-}x$. As shown in Fig. S9A and S9B, the morphology of $\text{AgInS}_2@\text{CeO}_2\text{-}x$ was basically not affected by visible light irradiation. The surface potential difference between AgInS_2 QDs (point a) and CeO_2 (point b) was about 51 mV in the dark

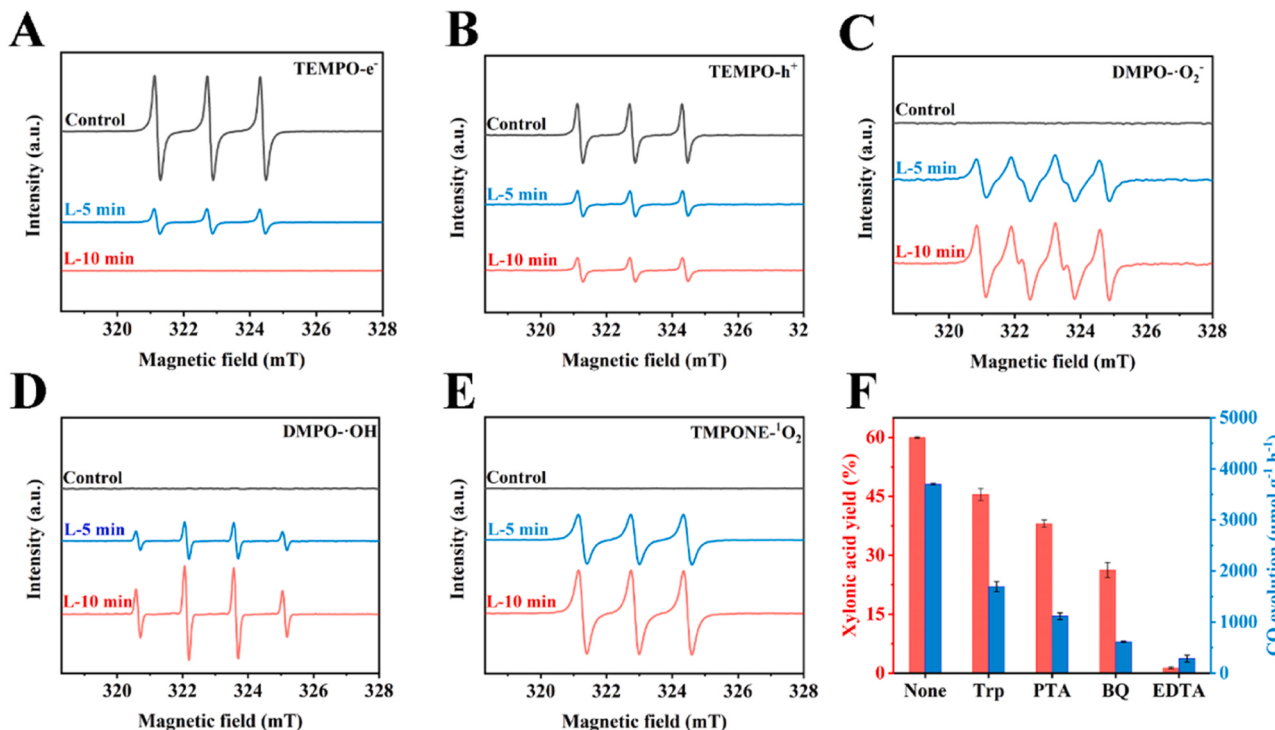


Fig. 6. TEMPO ESR spin-labelling of e^- (A) and h^+ (B), DMPO ESR spin-labelling of $\cdot\text{O}_2$ (C) and $\cdot\text{OH}$ (D), TEMPONE ESR spin-labelling of $^1\text{O}_2$ (E). The effects of different oxidation active species on the co-production of xylylic acid and CO from xylose through $\text{AgInS}_2@\text{CeO}_2\text{-}20$ photocatalysis (F).

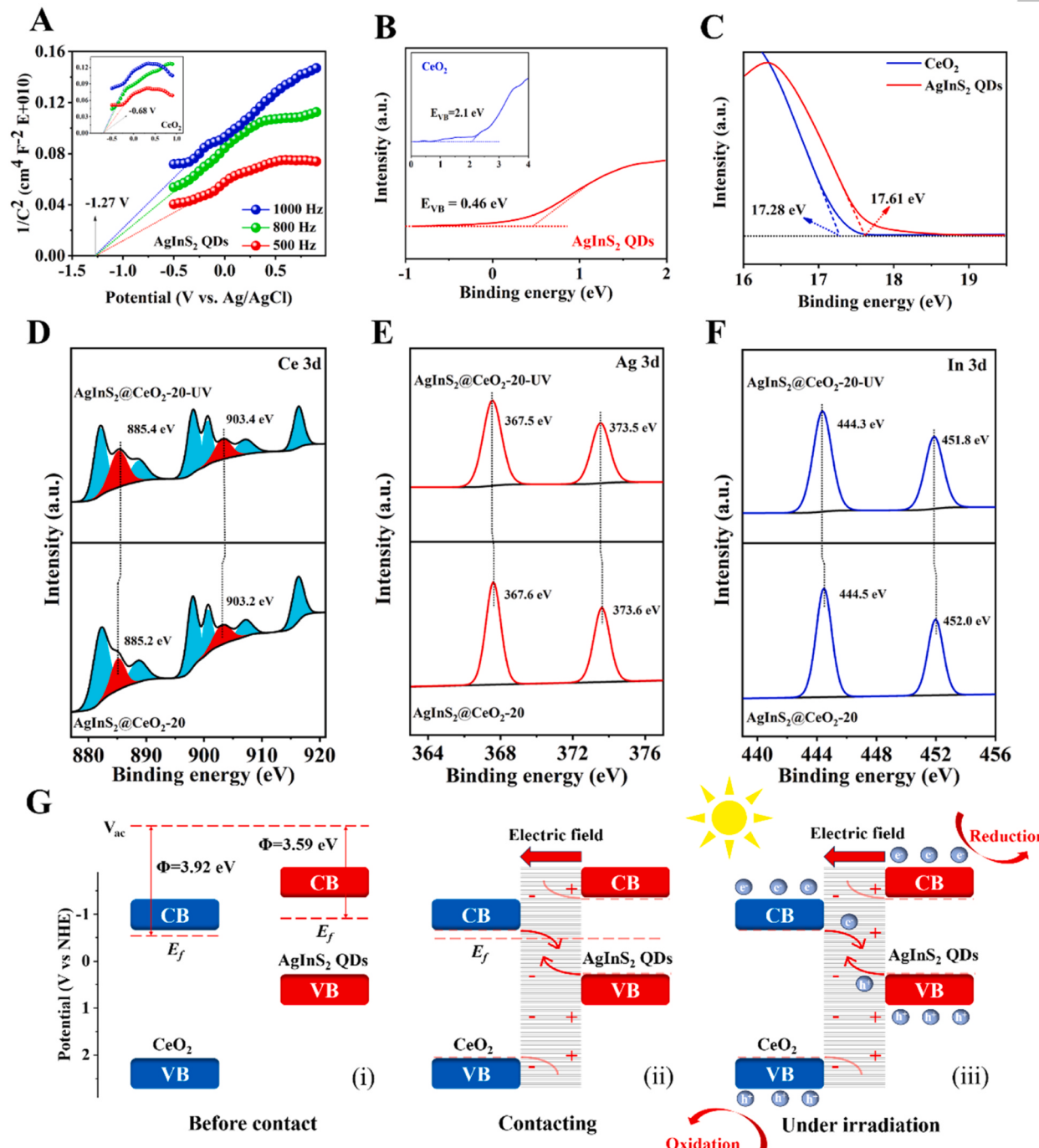
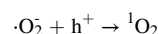
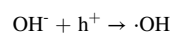
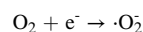
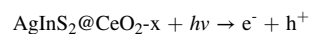


Fig. 7. The M-S plots (A), the valence band spectrum (B), and UPS (C) of CeO_2 and AgInS_2 QDs. The High-resolution XPS (In-situ) spectra of Ce 3d (D), Ag 3d (E), and In 3d (F) in the $\text{AgInS}_2@\text{CeO}_2$ -20. The schematic illustration of the S-scheme charge transfer mechanism of $\text{AgInS}_2@\text{CeO}_2$ -x heterostructure.

(Fig. S9C), indicating the formation of an interface electric field from point a to point b. Furthermore, the potential of point a in dark is -393 mV, which declines to -435 mV under the lights (Fig. S9E). The decrease (42 mV) of point a (AgInS_2 QDs) was much than that (13 mV) of point b (CeO_2) indicating the migration of photogenerated electrons from CeO_2 to AgInS_2 QDs [48]. This results further evidenced the formation of the S-scheme heterostructure between them. In summary, all the results confirm the formation of an S-scheme heterojunction in $\text{AgInS}_2@\text{CeO}_2$ -x.

According to previous reports [49], a possible conversion mechanism for xylose on $\text{AgInS}_2@\text{CeO}_2$ -x was proposed (Fig. 8). Initially, under visible light irradiation, e^- transition from the VB to the CB of

$\text{AgInS}_2@\text{CeO}_2$ -x, resulting in the formation of h^+ - e^- pairs. Subsequently, these h^+ - e^- pairs actively contribute to the generation of reactive oxygen species. The mechanism can be summarized as follows:



It is clear that CeO_2 is the main reactive active center in the

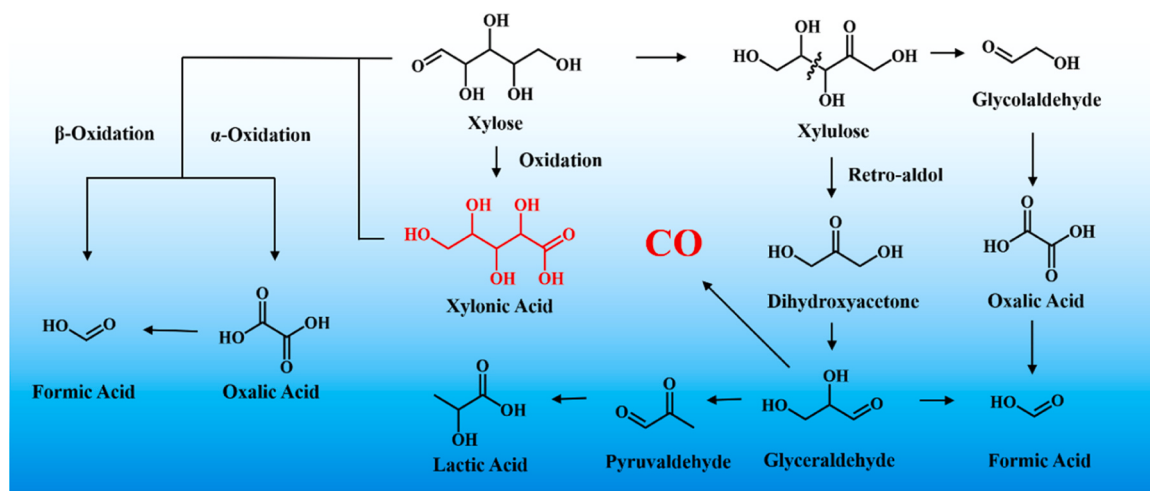


Fig. 8. The possible reaction pathway for photocatalytic co-production of xylonic acid and CO in xylose-alkaline system through AgInS₂@CeO₂-20 photocatalysis.

photocatalytic selective oxidation of xylose for the co-production of xylonic acid and CO. Firstly, the staggered band structures (Fig. 7G) of CeO₂ and AgInS₂ QDs were confirmed through Mott-Schottky (M-S) analysis, valence band spectrum, and ultraviolet photoelectron spectroscopy (UPS). CeO₂ served as an oxidation photocatalyst (OP) in an AgInS₂@CeO₂-x S-scheme heterojunction due to a more positive valence band position. Under light irradiation, the photo-generated e⁻ exists in the CB of CeO₂ and holes manifest in the VB of AgInS₂ QDs. As a result, highly reducing e⁻ in the CB of AgInS₂ QDs and highly oxidizing h⁺ in the VB of CeO₂ are retained, participating in reactions on the surface of the photocatalyst. Furthermore, various scavengers were injected to remove the oxidation active species, specifically, Trp for ¹O₂, PTA for ·OH, BQ for ·O₂[·], and EDTA for h⁺ in poisoning experiments. As shown in Fig. 6F, the yield of xylonic acid was trace (1.3%) and the CO evolution was 286.1 $\mu\text{mol g}^{-1} \text{h}^{-1}$, indicating that h⁺ played an important role in the selective oxidation of xylose. Finally, the large number of oxygen vacancies in CeO₂ was confirmed by XPS spectra and EPR spectra in this work. Under the positive influence of fast carrier separation and oxygen vacancies, the yield of xylonic acid and CO evolution was greatly increased. In summary, we consider CeO₂ as the main reactive active site in the reaction of selective oxidation of xylose for the co-production of xylonic acid and CO.

Regarding xylonic acid, it is considered the initial product resulting from the selective oxidation of xylose. Simultaneously, xylose and the generated xylonic acid undergo peroxidation to give oxalic acid through α -oxidation. Additionally, β -oxidation yield formic acid. Ultimately, partial formic acid was generated from oxalic acid. Furthermore, xylose can partly isomerize into xylulose, after which glycolaldehyde and dihydroxyacetone are formed through the cleavage of the C-C bond. These compounds then further transform into glycolaldehyde and glyceraldehyde. Subsequently, glyceraldehyde gives rise to CO and formic acid. Lactic acid is produced through the hydration process of pyruvaldehyde.

4. Conclusions

In conclusion, we successfully load AgInS₂ QDs onto CeO₂ to form S-scheme heterojunction and enhance oxygen defects via two-step hydrothermal and mild annealing processes. XPS and EPR analysis confirm the increase in oxygen vacancies. The E_f calculation, *situ* irradiated XPS results, and Kelvin probe force microscopy (KPFM) spectra confirm the S-scheme mechanism in AgInS₂@CeO₂-20. The AgInS₂@CeO₂-20 photocatalyst showed excellent performance (60.0% xylonic acid yield and 3689.9 $\mu\text{mol g}^{-1} \text{h}^{-1}$ CO evolution rate) at 60 °C in 0.1 M KOH under visible light irradiation, which are much higher than CeO₂ and AgInS₂

QDs. ESR results and poisoning experiments indicate the generation of reactive oxygen species and major role of h⁺. The possible pathways for the conversion of xylose to CO and xylonic acid have been proposed. This work provides a potential strategy to develop defects rich S-scheme photocatalysts for co-product xylonic acid and CO via biorefinery.

CRediT authorship contribution statement

Li Aohua: Writing – original draft, Software, Formal analysis, Data curation. **Ma Jiliang:** Writing – review & editing, Supervision, Methodology, Investigation, Funding acquisition, Data curation, Conceptualization. **Sun Runcang:** Writing – review & editing, Supervision. **Hong Min:** Supervision, Writing – review & editing.

Declaration of Competing Interest

The authors declare that they have no known competing financial interests or personal relationships that could have appeared to influence the work reported in this paper.

Data Availability

Data will be made available on request.

Acknowledgements

This work was supported by the National Natural Science Foundation of China (22008018, 22378035), Youth Talent Promotion Project of China Association for Science and Technology (YESS20210216), Dalian Outstanding Young Scientific and Technological Talents (2022RY24), Liaoning Province's "Xingliao Talent Plan" Youth Top Talents (XLYC2203010).

Appendix A. Supporting information

Supplementary data associated with this article can be found in the online version at doi:10.1016/j.apcatb.2024.123834.

References

- [1] V.S. Sikarwar, M. Zhao, P. Clough, J. Yao, X. Zhong, M.Z. Memon, N. Shah, E. J. Anthony, P.S. Fennell, An overview of advances in biomass gasification, *Energy Environ. Sci.* 9 (2016) 2939–2977.
- [2] R. Fang, A. Dhakshinamoorthy, Y.W. Li, H. Garcia, Metal organic frameworks for biomass conversion, *Chem. Soc. Rev.* 49 (2020) 3638–3687.
- [3] J.S.M. Samec, Holistic approach for converting biomass to fuels, *Chem* 4 (2018) 1199–1200.

[4] J.H. Xu, L.L. Wang, L.J. Sun, W.K. Wang, T.T. Kong, H.P. Jiang, Q.Q. Liu, Boosting photocatalytic synchronous production of H₂ coupled with acetone over Co doped Cu₃P quantum dots/ZnIn₂S₄ nanosheets p-n nanojunction, *J. Colloid Interf. Sci.* 646 (2024) 254–264.

[5] M. Wang, M.J. Liu, J.M. Lu, F. Wang, Photo splitting of bio-polymers and sugars to methanol and syngas, *Nat. Commun.* 11 (2020) 1083.

[6] M. Wang, H.R. Zhou, F. Wang, Photocatalytic production of syngas from biomass, *Acc. Chem. Res.* 56 (2023) 1057–1069.

[7] J. Lee, S. Jung, Y.T. Kim, H.J. Kim, K.H. Kim, Catalytic and electrocatalytic conversion of glucose into value-added chemicals, *Renew. Sust. Energ. Rev.* 181 (2023) 113337.

[8] M.S. Lekshmi Sundar, K. Madhavan, Nampoothiri, An overview of the metabolically engineered strains and innovative processes used for the value addition of biomass derived xylose to xylitol and xylonic acid, *Bioresour. Technol.* 345 (2022) 126548.

[9] M.S. Li, L.X. Zhong, W. Chen, Y.M. Huang, Z.X. Chen, D.Q. Xiao, R. Zou, L. Chen, Q. Hao, Z.H. Liu, R.C. Sun, X.W. Peng, Regulating the electron–hole separation to promote selective oxidation of biomass using ZnS@Bi₂S₃ nanosheet catalyst, *Appl. Catal. B-Environ.* 292 (2021) 120180.

[10] A.B. Bañares, G.M. Nisola, K.N.G. Valdehuesa, W.K. Lee, W.J. Chung, Understanding D-xyloonic acid accumulation: a cornerstone for better metabolic engineering approaches, *Appl. Microbiol. Biotechnol.* 105 (2021) 5309–5324.

[11] K.N. Liu, J.L. Ma, X.P. Yang, D.N. Jin, Y.C. Li, G.J. Jiao, S.Q. Yao, S.L. Sun, R. C. Sun, Boosting electron kinetics of anatase TiO₂ with carbon nanosheet for efficient photo-reforming of xylose into biomass-derived organic acids, *J. Alloy. Compd.* 906 (2022) 164276.

[12] J.Q. Zhang, K.N. Liu, S.L. Sun, R.C. Sun, J.L. Ma, Photo-splitting xylose and xylan to xylonic acid and carbon monoxide, *Green. Chem.* 24 (2022) 8367–8376.

[13] C.W. Sun, H. Li, L.Q. Chen, Nanostructured ceria-based materials: synthesis, properties, and applications, *Energy Environ. Sci.* 5 (2012) 8475–8505.

[14] Y.C. Zhang, Z. Li, L. Zhang, L. Pan, X.W. Zhang, L. Wang, A. Fazal e, J.J. Zou, Role of oxygen vacancies in photocatalytic water oxidation on ceria oxide: Experiment and DFT studies, *Appl. Catal. B-Environ.* 224 (2018) 101–108.

[15] S.M. Fang, Y.J. Xin, L. Ge, C.C. Han, P. Qiu, L.E. Wu, Facile synthesis of CeO₂ hollow structures with controllable morphology by template-engaged etching of Cu₂O and their visible light photocatalytic performance, *Appl. Catal. B-Environ.* 179 (2015) 458–467.

[16] X. Huang, K. Zhang, B. Peng, G. Wang, M. Muhler, F. Wang, Ceria-Based Materials for Thermocatalytic and Photocatalytic Organic Synthesis, *ACS Catal.* 11 (2021) 9618–9678.

[17] Y.Q. Lu, H. Deng, T.T. Pan, X. Liao, C.B. Zhang, H. He, Effective toluene ozonation over δ -MnO₂: oxygen vacancy-induced reactive oxygen species, *Environ. Sci. Technol.* 57 (2023) 2918–2927.

[18] S. Wei, H.X. Zhong, H.T. Wang, Y.J. Song, C.M. Jia, M. Anpo, L. Wu, Oxygen vacancy enhanced visible light photocatalytic selective oxidation of benzylamine over ultrathin Pd/BiOCl nanosheets, *Appl. Catal. B-Environ.* 305 (2022) 121032.

[19] C.H. Shen, Y. Chen, X.J. Xu, X. Li, X.J. Wen, Z.T. Liu, R. Xing, H. Guo, Z.H. Fei, Efficient photocatalytic H₂ evolution and Cr(VI) reduction under visible light using a novel Z-scheme SnIn₄S₈/CeO₂ heterojunction photocatalysts, *J. Hazard. Mater.* 416 (2021) 126217.

[20] Y.F. Wang, L. Yang, R. Zou, J.W. Lan, A.R. Yao, H.Y. Xiao, S.J. Lin, Z-scheme CeO₂/Ag/CdS heterojunctions functionalized cotton fibers as highly recyclable and efficient visible light-driven photocatalysts for the degradation of dyes, *J. Clean. Prod.* 380 (2022) 135012.

[21] Y. Shi, L. Li, Z. Xu, F. Guo, W. Shi, Construction of full solar-spectrum available S-scheme heterojunction for boosted photothermal-assisted photocatalytic H₂ production, *Chem. Eng. J.* 459 (2023) 141549.

[22] Q.L. Xu, L.Y. Zhang, B. Cheng, J.J. Fan, J.G. Yu, S-scheme heterojunction photocatalyst, *Chem* 6 (2020) 1543–1559.

[23] X.W. Ruan, C.X. Huang, H. Cheng, Z.Q. Zhang, Y. Cui, Z.Y. Li, T.F. Xie, K.K. Ba, H. Y. Zhang, L. Zhang, X. Zhao, J. Leng, S.Y. Jin, W. Zhang, W.T. Zheng, S.K. Ravi, Z. F. Jiang, X.Q. Cui, J.G. Yu, A twin S-scheme artificial photosynthetic system with self-assembled heterojunctions yields superior photocatalytic hydrogen evolution rate, *Adv. Mater.* 35 (2023) 2209141.

[24] L.Y. Zhang, J.J. Zhang, H.G. Yu, J.G. Yu, Emerging S-scheme photocatalyst, *Adv. Mater.* 34 (2022) 2107668.

[25] L. Zhao, J. Bian, X. Zhang, L. Bai, L. Xu, Y. Qu, Z. Li, Y. Li, L. Jing, Construction of ultrathin S-scheme heterojunctions of single Ni atom immobilized Ti-MOF and BiVO₄ for CO₂ photoconversion of nearly 100% to CO by pure water, *Adv. Mater.* 34 (2022) 2205303.

[26] Y. You, S.X. Chen, J. Zhao, J.F. Lin, D.L. Wen, P.Z. Sha, L.B. Li, D.L. Bu, S. M. Huang, Rational design of S-scheme heterojunction towards efficient photocatalytic cellulose reforming for H₂ and formic acid in pure water, *Adv. Mater.* (2023), <https://doi.org/10.1002/adma.202307962>.

[27] M.C. Nevárez Martínez, B. Bajorowicz, T. Klimczuk, A. Źak, J. Łuczak, W. Lisowski, A. Zaleska-Medynska, Synergy between AgInS₂ quantum dots and ZnO nanopyramids for photocatalytic hydrogen evolution and phenol degradation, *J. Hazrd. Mater.* 398 (2020) 123250.

[28] J.G. Du, S.L. Ma, H.P. Liu, H.C. Fu, L. Li, Z.Q. Li, Y. Li, J.G. Zhou, Uncovering the mechanism of novel AgInS₂ nanosheets/TiO₂ nanobelts composites for photocatalytic remediation of combined pollution, *Appl. Catal. B-Environ.* 259 (2019) 118062.

[29] P. Sun, Z.P. Xing, Z.Z. Li, W. Zhou, Recent advances in quantum dots photocatalysts, *Chem. Eng. J.* 458 (2023) 141399.

[30] K.L. Zhang, M. Zhou, K. Yang, C.L. Yu, P. Mu, Z.Z. Yu, K.Q. Lu, W.Y. Huang, W. X. Dai, Photocatalytic H₂O₂ production and removal of Cr (VI) via a novel Lu₃NbO₇; Yb, Ho/CQDs/AgInS₂/In₂S₃ heterostructure with broad spectral response, *J. Hazard. Mater.* 423 (2022) 127172.

[31] Y. Zhao, X. Fan, H. Zheng, E. Liu, J. Fan, X. Wang, Bi₂WO₆/AgInS₂ S-scheme heterojunction: Efficient photodegradation of organic pollutant and toxicity evaluation, *J. Mater. Sci. Technol.* 170 (2024) 200–211.

[32] L. Wang, R. Sa, Y. Wei, X. Ma, C. Lu, H. Huang, E. Fron, M. Liu, W. Wang, S. Huang, J. Hofkens, M.B.J. Roefers, Y.J. Wang, J. Wang, J. Long, X. Fu, R. Yuan, Near-infrared light-driven photoredox catalysis by transition-metal-complex nanodots, *Angew. Chem. Int. Ed.* 61 (2022) e202204561.

[33] L. Zhang, L. Zhang, G.C. Xu, C. Zhang, X. Li, Z.P. Sun, D.Z. Jia, Low-temperature CO oxidation over CeO₂ and CeO₂/Co₃O₄ core-shell microspheres, *New. J. Chem.* 41 (2017) 13418–13424.

[34] X.Y. Gu, C. Tan, L.X. He, J. Guo, X. Zhao, K.Z. Qi, Y. Yan, Mn²⁺ doped AgInS₂ photocatalyst for formaldehyde degradation and hydrogen production from water splitting by carbon tube enhancement, *Chemosphere* 304 (2022) 135292.

[35] J. Jin, J.G. Yu, D.P. Guo, C. Cui, W. Ho, A hierarchical Z-Scheme CdS-WO₃ photocatalyst with enhanced CO₂ reduction activity, *Small* 11 (2015) 5262–5271.

[36] X.Q. Wang, J.L. Wu, J.L. Wang, H.L. Xiao, B.X. Chen, R. Peng, M.L. Fu, L.M. Chen, D.Q. Ye, W. Wen, Methanol plasma-catalytic oxidation over CeO₂ catalysts: Effect of ceria morphology and reaction mechanism, *Chem. Eng. J.* 369 (2019) 233–244.

[37] X. Li, W.Q. Fan, Y.J. Bai, Y. Liu, F.F. Wang, H.Y. Bai, W.D. Shi, Photoelectrochemical reduction of nitrate to ammonia over CuPc/CeO₂ heterostructure: Understanding the synergistic effect between oxygen vacancies and Ce sites, *Chem. Eng. J.* 433 (2022) 133225.

[38] H.L. Tang, T.T. Ju, Y. Dai, M.L. Wang, Y.Q. Ma, M. Wang, G.H. Zheng, Ultrahigh efficiency CH₄ photocatalytic conversion to C1 liquid products over cheap and vacancy-rich CeO₂ at 30 °C, *J. Mater. Chem. A* 10 (2022) 18978–18988.

[39] R. Khatun, R.S. Pal, M.A. Shoeib, D. Khurana, S. Singh, N. Siddiqui, M.K. Poddar, T. S. Khan, R. Bal, Generation of active oxygen species by CO₂ dissociation over defect-rich Ni-Pt/CeO₂ catalyst for boosting methane activation in low-temperature dry reforming: Experimental and theoretical study, *Appl. Catal. B-Environ.* 340 (2024) 123243.

[40] R. Khatun, S. Bhandari, M.K. Poddar, C. Samanta, T.S. Khan, D. Khurana, R. Bal, Partial oxidation of methane over high coke-resistant bimetallic Pt-Ni/CeO₂ catalyst: Profound influence of Pt addition on stability, *Int. J. Hydrol. Energ.* 47 (2022) 38895–38909.

[41] M. Yao, Z.M. Tao, G.B. Liu, S.M. Li, Y. Zhang, A novel calcination method towards layered Ni-rich cathode with enhanced electrochemical performances and regulated oxygen vacancies, *Chem. Eng. J.* 473 (2023) 145090.

[42] J.Z. Qin, X. Hu, X.Y. Li, Z.F. Yin, B.J. Liu, K.-h. Lam, 0D/2D AgInS₂/MXene Z-scheme heterojunction nanosheets for improved ammonia photosynthesis of N₂, *Nano Energy* 61 (2019) 27–35.

[43] W.C. Wang, Y. Tao, J. Fan, Z. Yan, H. Shang, D.L. Phillips, M. Chen, G. Li, Fullerene-Graphene Acceptor Drives Ultrafast Carrier Dynamics for Sustainable CdS Photocatalytic Hydrogen Evolution, *Adv. Funct. Mater.* 32 (2022) 2201357.

[44] G.T. Sun, Z.G. Tai, F. Li, Q. Ye, T. Wang, Z. Fang, L.C. Jia, W. Liu, H.Q. Wang, Construction of ZnIn₂S₄/Cds/Pds S-scheme heterostructure for efficient photocatalytic H₂ production, *Small* 19 (2023) 2207758.

[45] Y. Zhang, Y.X. Wu, L. Wan, W.F. Yang, H.J. Ding, C.Y. Lu, W.H. Zhang, Z.P. Xing, Double Z-Scheme g-C₃N₄/BiOI/CdS heterojunction with I³⁻/I⁻ pairs for enhanced visible light photocatalytic performance, *Green. Energy Environ.* 7 (2022) 1377–1389.

[46] Z. Wei, W. Wang, W. Li, X. Bai, J. Zhao, E.C.M. Tse, D.L. Phillips, Y. Zhu, Steering electron-hole migration pathways using oxygen vacancies in tungsten oxides to enhance their photocatalytic oxygen evolution performance, *Angew. Chem. Int. Ed.* 60 (2021) 8236–8242.

[47] X.F. Ma, R. Xiao, Y. Wei, S. Zhang, X. Hu, L. Zhang, N. Qin, L. Wang, Z. Ding, H. Lin, Z. Zhang, J. Long, R. Yuan, Photothermal catalytic conversion of water and inert nitriles to amide activated by in-situ formed transition-metal-complex nanodots, *Appl. Catal. B-Environ.* 344 (2024) 123636.

[48] T. Ying, W. Liu, L. Yang, S. Zhang, Z. Wu, J. Li, R. Song, W. Dai, J. Zou, S. Luo, S-scheme construction boosts highly active self-supporting CeO₂/Cu₆O photocatalyst for efficient degradation of indoor VOCs, *Sep. Purif. Technol.* 330 (2024) 125272.

[49] Y.F. Zhang, H. Luo, L.Z. Kong, X.P. Zhao, G. Miao, L.J. Zhu, S.G. Li, Y.H. Sun, Highly efficient production of lactic acid from xylose using Sn-beta catalysts, *Green. Chem.* 22 (2020) 7333–7336.